Numer. Math. Theor. Meth. Appl.
doi: 10.4208/nmtma.OA-2022-0080

Vol. **16**, No. 1, pp. 182-203
February 2023

A Second-Order Semi-Implicit Method for the Inertial Landau-Lifshitz-Gilbert Equation

Panchi Li[1], Lei Yang[2], Jin Lan[3], Rui Du[1,4,*] and Jingrun Chen[1,4,5,6]

[1] *School of Mathematical Sciences, Soochow University, Suzhou 215006, China*
[2] *School of Computer Science and Engineering, Macau University of Science and Technology, Macao SAR, China*
[3] *Center for Joint Quantum Studies and Department of Physics, School of Science, Tianjin University, 92 Weijin Road, Tianjin 300072, China*
[4] *Mathematical Center for Interdisciplinary Research, Soochow University, Suzhou 215006, China*
[5] *Suzhou Institute for Advanced Research, University of Science and Technology of China, Suzhou, Jiangsu 215123, China*
[6] *School of Mathematical Sciences, University of Science and Technology of China, Hefei, Anhui 230026, China*

Received 11 May 2022; Accepted (in revised version) 31 July 2022

Abstract. Electron spins in magnetic materials have preferred orientations collectively and generate the macroscopic magnetization. Its dynamics spans over a wide range of timescales from femtosecond to picosecond, and then to nanosecond. The Landau-Lifshitz-Gilbert (LLG) equation has been widely used in micromagnetics simulations over decades. Recent theoretical and experimental advances have shown that the inertia of magnetization emerges at sub-picosecond timescales and contributes significantly to the ultrafast magnetization dynamics, which cannot be captured intrinsically by the LLG equation. Therefore, as a generalization, the inertial LLG (iLLG) equation is proposed to model the ultrafast magnetization dynamics. Mathematically, the LLG equation is a nonlinear system of parabolic type with (possible) degeneracy. However, the iLLG equation is a nonlinear system of mixed hyperbolic-parabolic type with degeneracy, and exhibits more complicated structures. It behaves as a hyperbolic system at sub-picosecond timescales, while behaves as a parabolic system at larger timescales spanning from picosecond to nanosecond. Such hybrid behaviors impose additional difficulties on designing efficient numerical methods for the iLLG equation. In this work, we propose a second-order semi-implicit scheme to solve the iLLG equation. The second-order temporal derivative of magnetization is approximated by the standard centered difference scheme, and the first-order temporal derivative is approximated by the midpoint scheme involving three time steps. The nonlinear terms are treated semi-implicitly using one-sided interpolation with second-order accuracy. At each time step, the unconditionally

*Corresponding author. *Email addresses:* leiyang@must.edu.mo (L. Yang), lanjin@tju.edu.cn (J. Lan), durui@suda.edu.cn (R. Du), jingrunchen@ustc.edu.cn (J. Chen), LiPanchi1994@163.com (P. Li)

unique solvability of the unsymmetric linear system is proved with detailed discussions on the condition number. Numerically, the second-order accuracy of the proposed method in both time and space is verified. At sub-picosecond timescales, the inertial effect of ferromagnetics is observed in micromagnetics simulations, in consistency with the hyperbolic property of the iLLG model; at nanosecond timescales, the results of the iLLG model are in nice agreements with those of the LLG model, in consistency with the parabolic feature of the iLLG model.

AMS subject classifications: 35Q99, 65Z05, 65M06

Key words: Inertial Landau-Lifshitz-Gilbert equation, semi-implicit scheme, second-order accuracy, micromagnetics simulations.

1. Introduction

Ferromagnetic materials are widely used for data storage devices due to the realization of fast magnetization dynamics under various external controls [4, 26]. In this scenario, the dissipative magnetization dynamics is mainly controlled by the magnetic degrees of freedom at timescales from picosecond (10^{-12} s) to nanosecond (10^{-9} s), which is typically modeled by the conventional Landau-Lifshitz-Gilbert (LLG) equation [10, 15]. However, some recent experiments including the observation of the spin dynamics at sub-picosecond timescales [2] as well as the realization of the magnetization reversal excited by the spin wave of sub-GHz frequency [11], indicated that ultrafast magnetic dynamics can be properly described by the LLG equation via adding an inertial term [3, 9, 18].

For the LLG equation with an inertial term, denoting τ as the characteristic timescale of the inertial effect, the magnetization dynamics can be roughly divided into two regimes: the diffusive regime at the timescale of $t \gg \tau$, and the hyperbolic regime at the timescale of $t \approx \tau$. In the hyperbolic regime, magnetization dynamics exhibits the inertial feature [17, 20]. From the modeling perspective, $\partial_t \mathbf{M}$ and $\mathbf{M} \times \partial_t \mathbf{M}$ control the time evolution of magnetization $\mathbf{M}(\mathbf{x}, t)$ in the LLG equation, and $\partial_{tt}\mathbf{M}$ is further added to account for the inertial effect. This modification leads to the inertial LLG (iLLG) equation [9, 18]. Mathematically, the LLG equation is a nonlinear system of equations of parabolic type with (possible) degeneracy. Under the condition $t \approx \tau$, the inertial term dominates and the iLLG equation is more like a nonlinear system of equations of hyperbolic type. While under the condition $t \gg \tau$, the inertial term can be ignored and the iLLG equation is more like a parabolic system. Therefore, a reliable numerical method for the iLLG equation should capture both the inertial dynamics at sub-picosecond timescales and the gyroscopic dynamics at nanosecond timescales.

There exist a large number of numerical methods for the LLG equation; see [8, 13] for reviews and references therein. First-order semi-implicit schemes such as the Gauss-Seidel projection method [16, 24] and the semi-implicit backward Euler method [7] are well established. And recently, a second order semi-implicit projection method with

backward differentiation formula was proposed with its second-order accuracy strictly proved [6, 25]. Closely related to the current work, the implicit midpoint scheme for the conventional LLG equation is available in the literature [1]. Its convergence and the energy dissipation are proved under the assumption that the nonlinear system of equations has a unique solution at each time step. However, for larger temporal stepsizes, the convergence of a nonlinear solver such as Netwon's method often slows down. Moreover, multiple solutions may arise in micromagnetics simulations if the initial guess is chosen arbitrarily [23]. Therefore, we focus on semi-implicit schemes in the current work.

However, numerical methods specific for the iLLG equation are rarely studied. In [21], the author provides the tangent plane scheme (TPS) with the first-order accuracy and the angular momentum method (AMM) with second-order accuracy. Through introducing $\mathbf{V} = \partial_t \mathbf{M}$ and $\mathbf{W} = \mathbf{M} \times \partial_t \mathbf{M}$, the iLLG equation is rewritten as the first-order systems. In AMM, $\mathbf{M}$ and $\mathbf{W}$ are treated as unknown fields to be approximated and thus the number of unknowns is doubled, and a full set of nonlinear equations has to be solved at each time step since the implicit midpoint scheme is applied for the temporal discretization. In our work, we propose a second-order semi-implicit scheme to solve the iLLG equation. The key idea is to apply the midpoint scheme with three time steps to approximate the first-order derivative $\partial_t \mathbf{M}$, and the centered difference scheme to approximate the second-order derivative $\partial_{tt} \mathbf{M}$ simultaneously, and then to make nonlinear terms semi-implicit using one-sided interpolation with magnetization at the previous time steps. We prove that the unsymmetric linear system of equations is unconditionally uniquely solvable at each time step. Specifically, the unsymmetric linear systems of equations are solved by the GMRES solver [5].

The rest of the paper is organized as follows. In Section 2, the formulation of the iLLG equation is introduced. In Section 3, the second-order semi-implicit scheme is proposed, and the unique solvability of the unsymmetric linear system is proved. In Section 4, the second-order accuracy in both space and time is checked numerically, and the dynamics of the iLLG equation is studied at different timescales. Conclusions are drawn in Section 5.

2. The inertial Landau-Lifshitz-Gilbert equation

The dynamics of magnetization $\mathbf{M}(\mathbf{x}, t)$ in a ferromagnetic medium is described by the classical LLG equation [10, 15]

$$\partial_t \mathbf{M} = -\gamma \mathbf{M} \times \left(\mathbf{H}_{\text{eff}} - \frac{\alpha}{\gamma M_s} \partial_t \mathbf{M} \right), \tag{2.1}$$

where γ is the gyromagnetic ratio, α is the Gilbert damping parameter, and $M_s = |\mathbf{M}|$ the saturation magnetization which is treated as a constant below the Curie temperature. The effective field $\mathbf{H}_{\text{eff}} = -\delta \mathcal{F} / \delta \mathbf{M}$ is defined as the variational derivative of the Landau-Lifshitz (LL) energy $\mathcal{F}$ with respect to magnetization $\mathbf{M}$, and the LL energy $\mathcal{F}$

reads as

$$\mathcal{F}[\mathbf{M}] = \int_\Omega \left[\frac{A}{M_s^2} |\nabla \mathbf{M}|^2 + \Phi\left(\frac{\mathbf{M}}{M_s}\right) - \mu_0 \mathbf{H}_\mathrm{e} \cdot \mathbf{M} \right] \mathrm{d}\mathbf{x} + \frac{\mu_0}{2} \int_{\mathbb{R}^3} |\nabla U|^2 \mathrm{d}\mathbf{x}, \tag{2.2}$$

where μ_0 denotes the permeability of vacuum, and Ω is the volume occupied by the material. On the right-hand side of (2.2), $\int_\Omega (A/M_s^2)|\nabla \mathbf{M}|^2 \mathrm{d}\mathbf{x}$ is the exchange energy, $\int_\Omega \Phi(\mathbf{M}/M_s)\mathrm{d}\mathbf{x}$ is the anisotropy energy, $-\mu_0 \int_\Omega \mathbf{H}_\mathrm{e} \cdot \mathbf{M} \mathrm{d}\mathbf{x}$ is the Zeeman energy resulting from the external magnetic field $\mathbf{H}_\mathrm{e}$, and the last term $(\mu_0/2)\int_{\mathbb{R}^3} |\nabla U|^2 \mathrm{d}\mathbf{x}$ is the dipolar energy from the stray field induced by the magnetization inhomogeneity and discontinuity. The dipolar energy can be alternatively written as $(-\mu_0/2)\int_\Omega \mathbf{H}_\mathrm{s} \cdot \mathbf{M} \mathrm{d}\mathbf{x}$, where $\mathbf{H}_\mathrm{s} = -\nabla U$ is the stray field and

$$U = \int_\Omega \nabla N(\mathbf{x} - \mathbf{y}) \cdot \mathbf{M}(\mathbf{y}) \mathrm{d}\mathbf{y}$$

with the Newtonian potential $N(\mathbf{x}) = -1/(4\pi|\mathbf{x}|)$. For simplicity, we assume that the material is uniaxial, i.e.,

$$\Phi\left(\frac{\mathbf{M}}{M_s}\right) = \frac{K_u\big(M_2^2 + M_3^2\big)}{M_s^2}$$

with K_u the anisotropy constant. Consequently, the total effective field reads as

$$\mathbf{H}_\mathrm{eff} = \frac{2A}{M_s^2}\Delta \mathbf{M} - \frac{2K_u}{M_s^2}(M_2 \mathbf{e}_2 + M_3 \mathbf{e}_3) + \mu_0 \mathbf{H}_\mathrm{e} + \mu_0 \mathbf{H}_\mathrm{s}, \tag{2.3}$$

where $\mathbf{e}_2 = (0,1,0)^T$, $\mathbf{e}_3 = (0,0,1)^T$.

Recent advances in experiments revealed the ultrafast inertial dynamics [17, 20] at sub-picosecond timescales that is beyond the scope of the classical LLG equation. To take account of the inertial effect, the iLLG equation is proposed as [3, 9, 18]

$$\partial_t \mathbf{M} = -\gamma \mathbf{M} \times \Big(\mathbf{H}_\mathrm{eff} - \frac{\alpha}{\gamma M_s}(\partial_t \mathbf{M} + \tau \partial_{tt} \mathbf{M}) \Big), \tag{2.4}$$

where τ represents the characteristic timescale of the inertial dynamics of magnetization. Note that the dynamics of magnetization in ferrimagnets and antiferromagnets with two sublattices $\mathbf{M}_1$ and $\mathbf{M}_2$ can be recast to the dynamics of stagger magnetization $\mathbf{p} = (\mathbf{M}_1 - \mathbf{M}_2)/(M_{s1} + M_{s2})$ and the net magnetization $\mathbf{q} = \mathbf{M}_1/M_{s1} + \mathbf{M}_2/M_{s2}$, and the dynamics of $\mathbf{p}$ follows a similar form of the dynamics governed by the iLLG equation [12, 14].

Proposition 2.1. *Define the total energy as*

$$\mathcal{J}[\mathbf{M}] = \mathcal{F}[\mathbf{M}] + \frac{\alpha\tau}{2\gamma M_s} \int_\Omega |\partial_t \mathbf{M}|^2 \mathrm{d}\mathbf{x}.$$

Then the following energy law holds

$$\frac{\mathrm{d}\mathcal{J}[\mathbf{M}]}{\mathrm{d}t} = -\frac{\alpha}{\gamma M_s} \int_\Omega |\partial_t \mathbf{M}|^2 \mathrm{d}\mathbf{x} - \mu_0 \int_\Omega \mathbf{M} \cdot \mathbf{H}_\mathrm{e}'(t) \mathrm{d}\mathbf{x}. \tag{2.5}$$

For the constant external magnetic field, the following energy dissipation relation holds as

$$\frac{d\mathcal{J}[\mathbf{M}]}{dt} = -\frac{\alpha}{\gamma M_s}\int_\Omega |\partial_t \mathbf{M}|^2 \mathrm{d}\mathbf{x} \le 0. \tag{2.6}$$

Proof. Taking the inner product of Eq. (2.4) and $(\mathbf{H}_{\text{eff}} - (\alpha/\gamma M_s)(\partial_t \mathbf{M} + \tau \partial_{tt}\mathbf{M}))$ yields

$$\int_\Omega \partial_t \mathbf{M} \cdot \Big(\mathbf{H}_{\text{eff}} - \frac{\alpha}{\gamma M_s}(\partial_t \mathbf{M} + \tau \partial_{tt}\mathbf{M})\Big)\mathrm{d}\mathbf{x} = 0. \tag{2.7}$$

Hence,

$$\begin{aligned}\frac{d\mathcal{J}[\mathbf{M}]}{dt} &= \int_\Omega \left\{ \big(\partial_t \mathbf{M} \cdot (-\mathbf{H}_{\text{eff}}) - \mu_0 \mathbf{M} \cdot \mathbf{H}_{\text{e}}'(t)\big) + \frac{\alpha\tau}{\gamma M_s}\partial_t \mathbf{M} \cdot \partial_{tt}\mathbf{M} \right\} \mathrm{d}\mathbf{x} \\ &\overset{(2.7)}{=} \int_\Omega \left\{ -\frac{\alpha}{\gamma M_s}|\partial_t \mathbf{M}|^2 - \mu_0 \mathbf{M} \cdot \mathbf{H}_{\text{e}}'(t) \right\} \mathrm{d}\mathbf{x},\end{aligned}$$

which completes the proof of Eq. (2.5). If $\mathbf{H}_{\text{e}}'(t)$ vanishes, the inequality (2.6) can be obtained directly from (2.5). □

Remark 2.1. To make the system well-posed, besides the governing equation (2.4) and the initial condition $\mathbf{M}(\mathbf{x}, 0) = \mathbf{M}_0$, one more initial condition related to the first-order temporal derivative $\partial_t \mathbf{M}(\mathbf{x}, 0)$ is needed. The following two different expressions (2.8) and (2.9) can be the option of the initial condition of $\partial_t \mathbf{M}(\mathbf{x}, 0)$

$$\partial_t \mathbf{M}(\mathbf{x}, 0) = \mathbf{0}, \tag{2.8}$$

$$\partial_t \mathbf{M}(\mathbf{x}, 0) = \mathbf{M} \times \mathbf{H}, \tag{2.9}$$

where $\mathbf{H}$ represents a field at $t = 0$. With the initial condition (2.9), the length of $\mathbf{M}$ can be preserved.

Different behaviors of nutation can be obtained from the different initial conditions (2.8) or (2.9); see a simple 1D case as below. Although it is feasible to adopt (2.9) as one of the initial conditions for the iLLG equation, it must be emphasized that the initial condition (2.8) is used throughout the paper unless otherwise specified, since the choice of the initial condition (2.9) instead of (2.8) would not impose any challenge on designing the numerical algorithm for the iLLG equation.

Here we consider the simplest system in which a single magnetization evolves under a uniform effective field. Consequently, the iLLG equation can be reduced to an ordinary differential equation (ODE)

$$d_t \mathbf{M} = -\mathbf{M} \times \big(\mathbf{H}_{\text{eff}} - \alpha(d_t \mathbf{M} + \tau d_{tt}\mathbf{M})\big). \tag{2.10}$$

When two different sets of the initial conditions

$$\begin{cases} \mathbf{M}(t = 0) = \mathbf{M}_0, \\ d_t \mathbf{M}(t = 0) = \mathbf{0}, \end{cases} \tag{2.11}$$

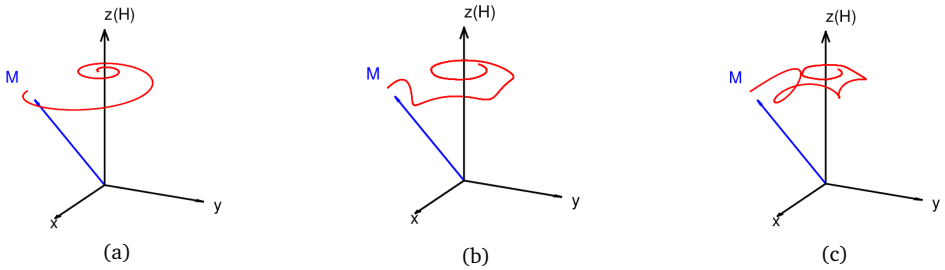

Figure 1: Numerical simulations of a single magnetization under a uniform effective field governed by (a) LLG equation and (b)-(c) iLLG equation. The blue arrows depict the initial magnetization, and the red lines plot the loci of the magnetization. The characteristic time of the inertial dynamics is $\tau = 0$ in (a) and $\tau = 2.0$ in (b)-(c). The initial conditions (2.11) are used in (b) and (2.12) in (c). Other parameters used in the simulations are: the Gilbert damping constant $\alpha = 0.2$, the effective field $\mathbf{H}_{\text{eff}} = (0, 0, 1)^T$ and the initial magnetization $\mathbf{M}_0 = (0, -1/\sqrt{2}, 1/\sqrt{2})^T$.

$$\begin{cases} \mathbf{M}(t=0) = \mathbf{M}_0, \\ d_t\mathbf{M}(t=0) = \mathbf{M} \times \mathbf{H} \end{cases} \tag{2.12}$$

are applied, different nutation loci are observed by solving the ODE (2.10) numerically, as shown in Fig. 1. The time-marching scheme provided in this paper is employed for the temporal discretization of the ODE, and the midpoint scheme [1] is employed for the temporal discretization of the second initial condition in (2.12). In numerical simulations, $\tau = 0$ and $\tau = 2.0$ correspond to the magnetization dynamics governed by the LLG equation and the iLLG equation, respectively. Other settings are: $\alpha = 0.2$, $\mathbf{H}_{\text{eff}} = (0, 0, 1)^T$ and $\mathbf{M}_0 = (0, -1/\sqrt{2}, 1/\sqrt{2})^T$.

For simplification, we rewrite the iLLG equation (2.4) in a dimensionless form by defining $\mathbf{H}_{\text{eff}} = \mu_0 M_s \mathbf{h}$, $\mathbf{H}_{\text{e}} = M_s \mathbf{h}_{\text{e}}$, $\mathbf{H}_{\text{s}} = M_s \mathbf{h}_{\text{s}}$, and $\mathbf{M} = M_s \mathbf{m}$. After the spatial rescaling $\mathbf{x} \to L\mathbf{x}$ (still use $\mathbf{x}$ after rescaling) with L being the diameter of Ω, the dimensionless form of the LL energy functional is

$$\tilde{\mathcal{F}}[\mathbf{m}] = \frac{1}{2}\int_{\Omega'} \Big[\epsilon|\nabla \mathbf{m}|^2 + q\big(m_2^2 + m_3^2\big) - 2\mathbf{h}_{\text{e}} \cdot \mathbf{m} - 2\mathbf{h}_{\text{s}} \cdot \mathbf{m}\Big] \mathrm{d}\mathbf{x}, \tag{2.13}$$

where

$$\epsilon = \frac{2A}{\mu_0 M_s^2 L^2}, \quad q = \frac{2K_u}{\mu_0 M_s^2}, \quad \tilde{\mathcal{F}}[\mathbf{m}] = \frac{\mathcal{F}[\mathbf{M}]}{\mu_0 M_s^2}.$$

Meanwhile, after the temporal rescaling $t \to t(M_s \mu_0 \gamma)^{-1}$ (still use t after rescaling), the dimensionless form of (2.4) reads as

$$\partial_t \mathbf{m} = -\mathbf{m} \times \mathbf{h} + \alpha \mathbf{m} \times (\partial_t \mathbf{m} + \eta \partial_{tt} \mathbf{m}) \tag{2.14}$$

with

$$\mathbf{h} = \epsilon \Delta \mathbf{m} - q(m_2 \mathbf{e}_2 + m_3 \mathbf{e}_3) + \mathbf{h}_{\text{e}} + \mathbf{h}_{\text{s}}. \tag{2.15}$$

The dimensionless parameter $\eta = \tau/(\mu_0 \gamma M_s)^{-1}$, represents the ratio between the characteristic timescale of the inertial dynamics and that of the gyroscopic magnetization

dynamics. For (2.14), homogeneous Neumann boundary condition is used as

$$\frac{\partial \mathbf{m}}{\partial \boldsymbol{\nu}}\Big|_{\partial\Omega} = 0, \tag{2.16}$$

where $\boldsymbol{\nu}$ represents the outward unit normal vector along boundary surface $\partial\Omega$.

3. A second-order semi-implicit finite difference scheme

Denote

$$\mathbf{f}(\mathbf{m}^n) = -q\big(m_2^n\mathbf{e}_2 + m_3^n\mathbf{e}_3\big) + \mathbf{h}_{\mathrm{e}}^n + \mathbf{h}_{\mathrm{s}}^n. \tag{3.1}$$

For (2.14)-(2.16), we employ a midpoint scheme with three time steps

$$\begin{aligned}
&\frac{\mathbf{m}^{n+1}-\mathbf{m}^{n-1}}{2\Delta t}\\
&= -\frac{\mathbf{m}^{n+1}+\mathbf{m}^{n-1}}{2}\times\left(\epsilon\Delta_h\frac{\mathbf{m}^{n+1}+\mathbf{m}^{n-1}}{2}+\mathbf{f}\left(\frac{\mathbf{m}^{n+1}+\mathbf{m}^{n-1}}{2}\right)\right)\\
&\quad+\alpha\frac{\mathbf{m}^{n+1}+\mathbf{m}^{n-1}}{2}\times\left(\frac{\mathbf{m}^{n+1}-\mathbf{m}^{n-1}}{2\Delta t}+\eta\frac{\mathbf{m}^{n+1}-2\mathbf{m}^{n}+\mathbf{m}^{n-1}}{\Delta t^2}\right),
\end{aligned} \tag{3.2}$$

where Δ_h represents the standard second-order centered difference stencil. For a 3D Cartesian mesh with indices $j = 0, 1, \ldots, n_x, n_x+1$, $k = 0, 1, \ldots, n_y, n_y+1$ and $l = 0, 1, \ldots, n_z, n_z+1$, the second-order centered difference for $\Delta_h\mathbf{m}_{j,k,l}$ reads

$$\begin{aligned}
\Delta_h\mathbf{m}_{j,k,l} = &\frac{\mathbf{m}_{j+1,k,l}-2\mathbf{m}_{j,k,l}+\mathbf{m}_{j-1,k,l}}{\Delta x^2}\\
&+\frac{\mathbf{m}_{j,k+1,l}-2\mathbf{m}_{j,k,l}+\mathbf{m}_{j,k-1,l}}{\Delta y^2}\\
&+\frac{\mathbf{m}_{j,k,l+1}-2\mathbf{m}_{j,k,l}+\mathbf{m}_{j,k,l-1}}{\Delta z^2},
\end{aligned} \tag{3.3}$$

where

$$\mathbf{m}_{j,k,l} = \mathbf{m}\left(\left(j-\frac{1}{2}\right)\Delta x, \left(k-\frac{1}{2}\right)\Delta y, \left(l-\frac{1}{2}\right)\Delta z\right).$$

For the Neumann boundary condition (2.16), a second-order approximation yields

$$\begin{aligned}
&\mathbf{m}_{0,k,l} = \mathbf{m}_{1,k,l}, \quad \mathbf{m}_{n_x,k,l} = \mathbf{m}_{n_x+1,k,l}, \quad k = 1,\ldots,n_y, \quad l = 1,\ldots,n_z,\\
&\mathbf{m}_{j,0,l} = \mathbf{m}_{j,1,l}, \quad \mathbf{m}_{j,n_y,l} = \mathbf{m}_{j,n_y+1,l}, \quad j = 1,\ldots,n_x, \quad l = 1,\ldots,n_z,\\
&\mathbf{m}_{j,k,0} = \mathbf{m}_{j,k,1}, \quad \mathbf{m}_{j,k,n_z} = \mathbf{m}_{j,k,n_z+1}, \quad j = 1,\ldots,n_x, \quad k = 1,\ldots,n_y.
\end{aligned}$$

In the above proposal, (3.2) is an implicit scheme with the truncation error $\mathcal{O}(h^2+\Delta t^2)$ with $\Delta x = \Delta y = \Delta z = h$, and hence a nonlinear system of equations has to be solved at each time step. In addition, for micromagnetics simulations, the evaluation

of the stray field $\mathbf{h}_{\mathrm{s}}^{n+1}$ is also computationally expensive. To overcome these issues, we propose the following second-order semi-implicit scheme:

$$\begin{cases} \dfrac{\tilde{\mathbf{m}}^{n+1}-\mathbf{m}^{n-1}}{2\Delta t} \\ = -\mathbf{m}^n \times \left(\epsilon\Delta_h\left(\dfrac{\tilde{\mathbf{m}}^{n+1}+\mathbf{m}^{n-1}}{2}\right)+\mathbf{f}(\mathbf{m}^n)\right) \\ \qquad +\alpha\mathbf{m}^n \times \left(\dfrac{\tilde{\mathbf{m}}^{n+1}-\mathbf{m}^{n-1}}{2\Delta t}+\eta\dfrac{\tilde{\mathbf{m}}^{n+1}-2\mathbf{m}^n+\mathbf{m}^{n-1}}{\Delta t^2}\right), & \text{(3.4a)} \\ \mathbf{m}^{n+1}=\dfrac{1}{|\tilde{\mathbf{m}}^{n+1}|}\tilde{\mathbf{m}}^{n+1}. & \text{(3.4b)} \end{cases}$$

By rewriting (3.4), at each time step, only a linear system of equations with the unsymmetric structure needs to be solved

$$\begin{aligned} &\left(I+\epsilon\Delta t\mathbf{m}^n\times\Delta_h-\alpha\left(1+\frac{2\eta}{\Delta t}\right)\mathbf{m}^n\times\right)\tilde{\mathbf{m}}^{n+1} \\ &=\mathbf{m}^{n-1}-\epsilon\Delta t\mathbf{m}^n\times\Delta_h\mathbf{m}^{n-1}-\alpha\left(1-\frac{2\eta}{\Delta t}\right)\mathbf{m}^n\times\mathbf{m}^{n-1} \\ &\quad -2\Delta t\mathbf{m}^n\times\mathbf{f}(\mathbf{m}^n). \end{aligned} \tag{3.5}$$

Consequently, to update $\mathbf{m}^{n+1}$, only $\mathbf{h}_{\mathrm{s}}^n$ at the previous step is needed.

Following [25], we establish the unique solvability of the proposed scheme (3.4) as follows. First, the unique solvability of (3.5) is given by the following proposition.

Proposition 3.1. *Denote*

$$S=\epsilon\Delta t\Delta_h-\alpha\left(1+\frac{2\eta}{\Delta t}\right)I,$$

I the identity operator, and $A=\mathbf{m}^n\times$ (rewritten in a matrix form) an antisymmetric matrix. Given $\mathbf{m}^{n-1}$ and $\mathbf{m}^n$, then $\det(I+AS)\neq 0$, i.e., (3.5) *admits a unique solution for any positive h and Δt.*

Proof. Since Δ_h is a symmetric positive definite matrix, there exists a nonsingular matrix C such that $\Delta_h=C^TC$. For the coefficient matrix $I+AS$ in (3.5), we have

$$\det(I+AS)=\det\left(I+AC^TC\right)=\det\left(I+CAC^T\right).$$

The matrix A is antisymmetric, so is CAC^T. The eigenvalues of CAC^T are either 0 or pure imaginary. Hence $\det(I+AS)\neq 0$, which is independent of h and Δt. □

Second, in (3.4), a projection step is applied after solving (3.5). The following proposition guarantees that the denominator is always nonzero.

Proposition 3.2. *If $\mathbf{m}^0 \cdot \mathbf{m}^1 \neq 0$ in the pointwise sense, then $|\tilde{\mathbf{m}}^n| \neq 0$ at any step n.*

Proof. Multiplying both sides of Eq. (3.4a) by $\mathbf{m}^n$ produces

$$\tilde{\mathbf{m}}^{n+1} \cdot \mathbf{m}^n = \mathbf{m}^n \cdot \mathbf{m}^{n-1}.$$

When $n = 1$, we have $\tilde{\mathbf{m}}^2 \cdot \mathbf{m}^1 = \mathbf{m}^1 \cdot \mathbf{m}^0 \neq 0$, which implies $|\tilde{\mathbf{m}}^2| \neq 0$. When $n = 2$, we have $\tilde{\mathbf{m}}^3 \cdot \mathbf{m}^2 = \mathbf{m}^2 \cdot \mathbf{m}^1 = \frac{1}{|\tilde{\mathbf{m}}^2|}\mathbf{m}^1 \cdot \mathbf{m}^0 \neq 0$, which implies $|\tilde{\mathbf{m}}^3| \neq 0$. Repeating this process completes the proof. □

Numerically, the initial condition (2.8) or (2.9) is discretized firstly. (2.8) leads to $\mathbf{m}^0 = \mathbf{m}^1$, i.e., $\mathbf{m}^0 \cdot \mathbf{m}^1 = 1$. For (2.9), we use the mid-point scheme and also have $\mathbf{m}^0 \cdot \mathbf{m}^1 \neq 0$.

Remark 3.1. After time rescaling $t \to (1 + \alpha^2)t$, (2.14) is equivalent to the LL form

$$\partial_t \mathbf{m} = -\mathbf{m} \times (\mathbf{h} - \tilde{\eta}\partial_{tt}\mathbf{m}) - \alpha \mathbf{m} \times \big(\mathbf{m} \times (\mathbf{h} - \tilde{\eta}\partial_{tt}\mathbf{m})\big), \tag{3.6}$$

where $\tilde{\eta} = \alpha\eta/((1 + \alpha^2)^2)$. The corresponding second-order semi-implicit scheme reads as

$$\begin{cases} \dfrac{\tilde{\mathbf{m}}^{n+1} - \mathbf{m}^{n-1}}{2\Delta t} \\ = -\mathbf{m}^n \times \left(\epsilon \Delta_h \left(\dfrac{\tilde{\mathbf{m}}^{n+1} + \mathbf{m}^{n-1}}{2} \right) - \tilde{\eta} \dfrac{\tilde{\mathbf{m}}^{n+1} - 2\mathbf{m}^n + \mathbf{m}^{n-1}}{\Delta t^2} + \mathbf{f}(\mathbf{m}^n) \right) \\ \quad -\alpha \mathbf{m}^n \times \left(\mathbf{m}^n \times \left(\epsilon \Delta_h \left(\dfrac{\tilde{\mathbf{m}}^{n+1} + \mathbf{m}^{n-1}}{2} \right) \right. \right. \\ \qquad \left. \left. -\tilde{\eta} \dfrac{\tilde{\mathbf{m}}^{n+1} - 2\mathbf{m}^n + \mathbf{m}^{n-1}}{\Delta t^2} + \mathbf{f}(\mathbf{m}^n) \right) \right), \\ \mathbf{m}^{n+1} = \dfrac{1}{|\tilde{\mathbf{m}}^{n+1}|} \tilde{\mathbf{m}}^{n+1}. \end{cases} \tag{3.7}$$

Next, we discuss how to solve the linear systems of equations in (3.5). Due to the unsymmetric structure, the GMRES solver is employed. The convergence of GMRES depends on the condition number of the linear system [22]. In the following, we provide a heuristic demonstration about how the condition number depends on the damping parameter α and the characteristic timescale of the inertial effect τ.

For simplicity, consider $\mathbf{m}^n = \mathbf{e}_1 = (1, 0, 0)^T$. In 1D, for the homogeneous Neumann boundary condition, the eigenvalues of Δ_x are

$$-\frac{4}{\Delta x^2} \sin^2 \left(\frac{j\pi \Delta x}{2} \right), \quad j = 1, \ldots, n_x,$$

and the eigenvalues of S are

$$\lambda_j = -\frac{4\epsilon \Delta t}{\Delta x^2} \sin^2 \left(\frac{j\pi \Delta x}{2} \right) - \alpha \left(1 + \frac{2\eta}{\Delta t} \right),$$

respectively. Therefore, the $3n_x$ eigenvalues of the antisymmetric matrix

$$\mathbf{e}_1 \times S = \begin{pmatrix} 0 & 0 & 0 \\ 0 & 0 & -S \\ 0 & S & 0 \end{pmatrix}$$

are

$$\underbrace{0, \cdots, 0}_{n_x}, \underbrace{\pm\lambda_1 i, \cdots, \pm\lambda_{n_x} i}_{n_x}.$$

Consequently, the eigenvalues of $(I + \epsilon\Delta t \mathbf{m}^n \times \Delta_x - \alpha(1 + 2\eta/\Delta t)\mathbf{m}^n\times)$ are

$$\underbrace{1, \cdots, 1}_{n_x}, 1 \pm \lambda_1 i, \cdots, 1 \pm \lambda_{n_x} i.$$

The condition number of $(I + \epsilon\Delta t \mathbf{m}^n \times \Delta_x - \alpha(1 + 2\eta/\Delta t)\mathbf{m}^n\times)$ is

$$\kappa = \sqrt{1 + \left(\frac{4\epsilon\Delta t}{\Delta x^2} + \alpha\left(1 + \frac{2\eta}{\Delta t}\right)\right)^2}. \tag{3.8}$$

Similarly, for a three dimensional cuboid domain and the same Neumann boundary condition, the eigenvalues of Δ_h are

$$\lambda_{jkl} = -\frac{4}{\Delta x^2}\sin^2\left(\frac{j\pi\Delta x}{2}\right) - \frac{4}{\Delta y^2}\sin^2\left(\frac{k\pi\Delta y}{2}\right) - \frac{4}{\Delta z^2}\sin^2\left(\frac{l\pi\Delta z}{2}\right),$$

and the condition number of $(I + \epsilon\Delta t \mathbf{m}^n \times \Delta_h - \alpha(1 + 2\eta/\Delta t)\mathbf{m}^n\times)$ is

$$\kappa = \sqrt{1 + \left[4\epsilon\Delta t\left(\frac{1}{\Delta x^2} + \frac{1}{\Delta y^2} + \frac{1}{\Delta z^2}\right) + \alpha\left(1 + \frac{2\eta}{\Delta t}\right)\right]^2}. \tag{3.9}$$

Fixing the space meshsizes and the time stepsize, the relation $\kappa^2 \sim \alpha\eta^2$ apparently holds for both (3.8) and (3.9). In our 3D micromagnetics simulations, material parameters can be found in Section 4.2. The number of iterations in GMRES is recorded for different combinations of α and τ in Table 1. It can be seen that for smaller α and τ, a smaller number of iterations is needed in GMRES.

Table 1: Number of iterations for GMRES at a single time step for different combinations of damping parameter α and inertial parameter τ. A ferromagnet of $200\ \mathrm{nm} \times 100\ \mathrm{nm} \times 5\ \mathrm{nm}$ is discretized into cells of $4\ \mathrm{nm} \times 4\ \mathrm{nm} \times 5\ \mathrm{nm}$. The crucial settings include: the initial magnetization $\mathbf{m}^0 = \mathbf{e}_1$, the time stepsize $\Delta t = 0.1\ \mathrm{ps}$, and the stopping tolerance $tol = 1.0 \times 10^{-11}$.

Number of iterations: Damping \ Inertial	$\tau = 1.0 \times 10^{-13}$ s ($\eta \approx 1.77 \times 10^{-2}$)	$\tau = 1.0 \times 10^{-11}$ s ($\eta \approx 1.77$)
$\alpha = 0.1$	9	9
$\alpha = 0.01$	7	11
$\alpha = 0.001$	6	9

4. Numerical results

In the numerical experiments, we first verify the second-order accuracy spatially and temporally for both 1D and 3D cases. For comparison, the full iLLG equation is simplified to

$$\partial_t \mathbf{m} = -\mathbf{m} \times \Delta \mathbf{m} + \alpha \mathbf{m} \times (\partial_t \mathbf{m} + \eta \partial_{tt} \mathbf{m}) + \mathbf{g}, \tag{4.1}$$

where $\mathbf{g}$ is the source term which can be generated by an exact solution $\mathbf{m}_{\rm e}$. In other words, when $\mathbf{m}$ is set as a given form $\mathbf{m}_{\rm e}$, the source term $\mathbf{g}$ will be generated correspondingly. The L^∞ error $\|\mathbf{m}_{\rm e} - \mathbf{m}_{\rm h}\|_\infty$ is recorded with $\mathbf{m}_{\rm e}$ and $\mathbf{m}_{\rm h}$ being the exact and the numerical solutions, respectively.

4.1. Accuracy check

Consider the exact solution of Eq. (4.1) in 1D case given as

$$\mathbf{m}_{\rm e} = \big(\cos(\bar{x})\sin(t^2), \sin(\bar{x})\sin(t^2), \cos(t^2)\big)^T$$

with $\bar{x} = x^2(1-x)^2$. The accompanying source term is

$$\mathbf{g} = \partial_t \mathbf{m}_{\rm e} + \mathbf{m}_{\rm e} \times \partial_{xx} \mathbf{m}_{\rm e} - \alpha \mathbf{m}_{\rm e} \times (\partial_t \mathbf{m}_{\rm e} + \eta \partial_{tt} \mathbf{m}_{\rm e}).$$

As shown in Table 2, the second-order accuracy is obtained in both time and space.

Table 2: The L^∞ errors for different space meshsizes and time stepsizes in 1D. The space meshsize used in temporal accuracy check is $\Delta x = 1.\text{e-}03$, and the time stepsize used in spatial accuracy check is $\Delta t = 2.5\text{e-}04$. The spatial points are $n_x = 1/\Delta x$, and the temporal steps are $n_t = T/\Delta t$.

$\eta = 0, \quad T = 0.05$							
$\alpha = 0.0$ $\eta = 0.0$	Space	n_x	80	160	320	640	Order
		error	1.75e-08	4.50e-09	1.12e-09	2.61e-10	2.02
	Time	n_t	80	160	320	640	Order
		error	1.79e-08	4.37e-09	1.01e-09	2.37e-10	2.08
$\alpha = 0.01$ $\eta = 0.0$	Space	n_x	80	160	320	640	Order
		error	1.75e-08	4.49e-09	1.12e-09	2.61e-10	2.02
	Time	n_t	80	160	320	640	Order
		error	1.78e-08	4.35e-09	1.01e-09	2.35e-10	2.08
$\eta \neq 0, \quad T = 0.5$							
$\alpha = 0.01$ $\eta = 100.0$	Space	n_x	80	160	320	640	Order
		error	1.60e-06	3.98e-07	9.69e-08	2.19e-08	2.06
	Time	n_t	80	160	320	640	Order
		error	2.45e-06	6.06e-07	1.45e-07	3.19e-08	2.09
$\alpha = 0.01$ $\eta = 1000.0$	Space	n_x	80	160	320	640	Order
		error	7.41e-07	1.99e-07	5.09e-08	1.21e-08	1.98
	Time	n_t	80	160	320	640	Order
		error	9.99e-07	2.48e-07	6.16e-08	1.53e-08	2.01

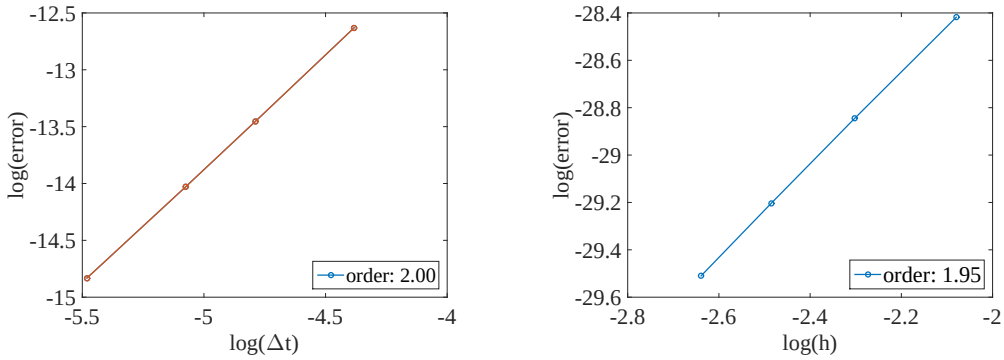

(a) Temporal accuracy (b) Spatial accuracy

Figure 2: The log-log plots of the L^∞ error in terms of (a) time stepsize Δt for temporal accuracy check and (b) space meshsize h for spatial accuracy check in 3D. The second-order accuracy is obtained in both time and space.

Next, we consider the exact solution in 3D case

$$\mathbf{m}_\mathrm{e} = \big(\cos(\bar{x}\bar{y}\bar{z})\sin(t^2), \sin(\bar{x}\bar{y}\bar{z})\sin(t^2), \cos(t^2)\big)^T$$

with $\bar{y} = y^2(1-y)^2$ and $\bar{z} = z^2(1-z)^2$. The corresponding source term is $\mathbf{g} = \partial_t \mathbf{m}_\mathrm{e} + \mathbf{m}_\mathrm{e} \times \Delta \mathbf{m}_\mathrm{e} - \alpha \mathbf{m}_\mathrm{e} \times (\partial_t \mathbf{m}_\mathrm{e} + \eta \partial_{tt} \mathbf{m}_\mathrm{e})$. To check the temporal accuracy, the magnetic element $\Omega = [0,1]^3$ is discretized uniformly with 10 mesh grids along each direction and the terminal time is $T = 0.5$. To check the spatial accuracy, $\Omega = [0,1]^3$ is discretized uniformly with $8, 10, 12, 14$ grid points along each direction, respectively, and the terminal time is $T = 0.02$ with the time stepsize $\Delta t = 1.0\text{e-}04$. The damping parameter α and the inertial parameter η are 0.01 and 1000, respectively. Fig. 2 plots the L^∞ error in terms of both the time stepsize and the space gridsize in 3D. The second-order accuracy is also obtained in both time and space.

4.2. Micromagnetics simulations

In this part, the ultrafast magnetization dynamics by using the full iLLG equation is studied numerically to investigate the inertial effect of ferromagnets. In the simulations, the magnetization is initialized with $\mathbf{m}^1 = \mathbf{m}^0 = \mathbf{e}_1$ and thus $\partial_t \mathbf{m}^0 = \mathbf{0}$ is automatically satisfied. This setup is physically reasonable for ferromagnetic materials in equilibrium with no external field applied. To highlight the role of the inertial term, we at first neglect the stray field since the contribution of the stray field usually dominates the LL energy in micromagnetics simulations. Then the stray field will be involved in the subsequent simulations to study the magnetization dynamics under an external magnetic field with GHz frequency.

In the first test, parameters of the ferromagnetic sample are: the total volume is $200\ \mathrm{nm} \times 100\ \mathrm{nm} \times 5\ \mathrm{nm}$ with the meshsize $4\ \mathrm{nm} \times 4\ \mathrm{nm} \times 5\ \mathrm{nm}$, the damping constant $\alpha = 0.02$, the saturation magnetization $M_s = 8.0 \times 10^5\ \mathrm{A/m}$, the exchange coupling

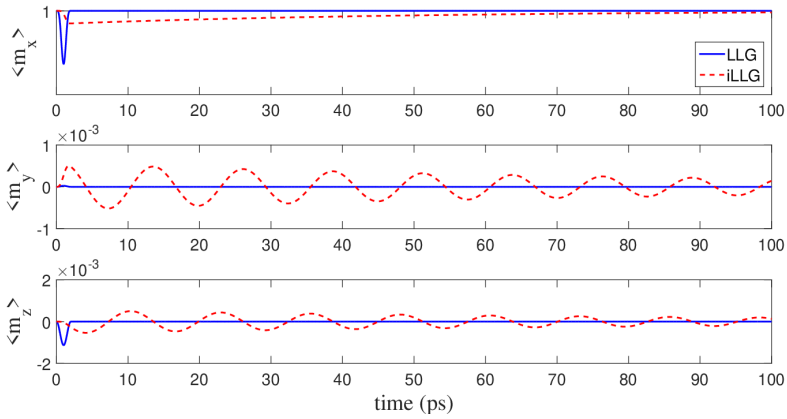

Figure 3: Evolution of the spatially averaged magnetization under a magnetic field pulse. The solid and dotted lines plot the averaged magnetizations of LLG and iLLG equations, respectively. A magnetic field pulse is applied along the $\mathbf{e}_2$ direction during $0 \sim 2$ ps to initiate the magnetization dynamics. The basic material parameters are: the characteristic inertial time $\tau = 1.0 \times 10^{-10}$ s, the damping constant $\alpha = 0.02$ and the time stepsize $\Delta t = 10$ fs.

constant $A = 1.3 \times 10^{-11}$ J/m, and the uniaxial anisotropy $K_u = 5.0 \times 10^2$ J/m^3 [20]. The dimensionless parameters are estimated as $\epsilon \sim \mathcal{O}(10^{-4})$, $q \sim \mathcal{O}(10^{-3})$, and $\eta \sim \mathcal{O}(10^{-1})$ when $\tau = 1.0 \times 10^{-12}$ s. It somehow explains that η is set to be 1000 when $\epsilon = 1$ in Section 4.1. A magnetic pulse $\mathbf{H}_{\rm e} = M_s F(t)\mathbf{e}_2$ is applied along the $\mathbf{e}_2$ direction with $F(t) = 0.01 \sin(2\pi f t)\chi_{0 \le t \le 2.0 \times 10^{-12}}$ and $f = 500$ GHz [21]. In Fig. 3, the components of the spatially averaged magnetization as functions of time are shown with the characteristic time $\tau = 1.0 \times 10^{-10}$ s, the total simulation time $T = 100$ ps, and the time stepsize $\Delta t = 10$ fs. From Fig. 3, remarkable different numerical results produced by the two governing equations can be observed. For the iLLG equation where the inertial term is present, oscillations of magnetization along the $\mathbf{e}_2$ and $\mathbf{e}_3$ directions can be observed much easier, which is the typical feature of the inertial dynamics. Fig. 4 shows the LL energies (without the dipolar energy term) as functions of time for the LLG equation and the iLLG equation when a magnetic field pulse is applied. It can be seen that the magnetization dynamics governed by the iLLG equation exhibits more significant response to the applied magnetic field pulse, which reveals that the inertial dynamics arises at sub-picosecond and picosecond timescales.

Although the inertial effect has been observed on the spatially averaged magnetization, it is of no significant effect on the LL energy in the absence of the dipolar energy. It means that the stable states of the system remain unchanged after the relaxation of inertial effect ends. In this sense, when the stray field is turned on, it is reasonable to infer that the equilibrium states generated by the iLLG equation are the same as those generated by the LLG equation. This inference is demonstrated in Fig. 5. Here the ferromagnet is of the size $2\ \mu\text{m} \times 1\ \mu\text{m} \times 0.02\ \mu\text{m}$ with the meshsize $20\ \text{nm} \times 20\ \text{nm} \times 20\ \text{nm}$, $\tau = 1.0 \times 10^{-10}$ s, and $T = 2$ ns with $\Delta t = 10$ fs. The basic material parameters can be found in the Standard Problem #1 [19].

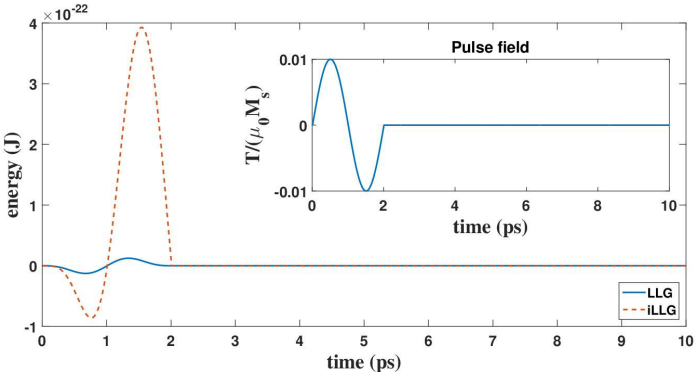

Figure 4: Evolution of the LL energy under a magnetic field pulse. The stray field is turned off, and the initial magnetic profile is the homogeneous magnetization along $\mathbf{e}_1$. Inset: profile of the magnetic field pulse, which takes a sine form during $0 \sim 2$ ps. The basic material parameters are the same as those used in Fig. 3.

Furthermore, following the study of hysteresis loops (see the standard specification stated in [19]), we simulate the magnetization dynamics using the iLLG equation with two sets of damping parameters and inertial parameters; see Fig. 6. For comparison, we list the coercive fields and remanent magnetizations for NIST (mo96a) and our simulations. We change the applied field by 0.5 mT each time from -50 mT to 50 mT, and then from 50 mT to -50 mT again. If the applied magnetic field is changed, a new steady state is considered to be reached when the relative change in the total energy is less than 1.0×10^{-7}.

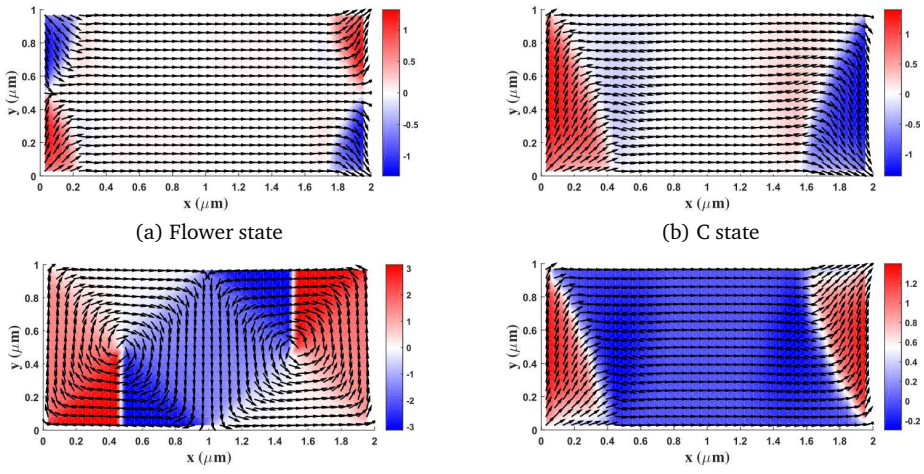

(a) Flower state (b) C state

(c) Diamond state (d) S state

Figure 5: Local stable states produced by the iLLG equation. For convenience of comparison with results obtained by the LLG equations (e.g., see [23, Fig. 2]), the ferromagnet is of the size $2\ \mu\text{m} \times 1\ \mu\text{m} \times 0.02\ \mu\text{m}$ with the following material parameters: the exchange coupling constant $A = 1.3 \times 10^{-11}$ J/m, the saturation magnetization $M_s = 8.0 \times 10^5$ A/m, the anisotropy $K_u = 5.0 \times 10^2$ J/m^3, the damping constant $\alpha = 0.1$, and the characteristic inertial time $\tau = 1.0 \times 10^{-10}$ s. The arrow represents the in-plane magnetization and the background color encodes the angle between the in-plane magnetization and the x-axis.

The main results of NIST (mo96a) and our simulations are:

- LLG equation (mo96a): coercive field x-loop/y-loop: 2.5/4.9 mT; remanent magnetization (m_x, m_y, m_z): x-loop: (0.15, 0.87, 0.00), y-loop: (-0.15, 0.87, 0.00).
- iLLG equation ($\alpha = 0.1$, $\tau = 1.0 \times 10^{-12}$ s and $\Delta t = 1$ ps): coercive field x-loop/y-loop: 2.3/5.3 mT; remanent magnetization (m_x, m_y, m_z): x-loop: (0.20, 0.87, 0.11e-04), y-loop: (-0.15, 0.88, 0.14e-04).
- iLLG equation ($\alpha = 0.02$, $\tau = 1.0 \times 10^{-13}$ s and $\Delta t = 0.1$ ps): coercive field x-loop/y-loop: 2.3/6.3 mT; remanent magnetization (m_x, m_y, m_z): x-loop: (0.20, 0.87, 0.25e-03), y-loop: (-0.14, 0.88, 0.86e-05).

The maximum deviations of coercive fields and components of the remanent magnetizations are 1.4 mT and 0.05, respectively. Qualitative agreements in terms of both coercive fields and remanent magnetizations confirm the consistency of the LLG and iLLG equations in long-term simulations.

In the previous simulations, we use the meshsize $20\ \mathrm{nm} \times 20\ \mathrm{nm} \times 20\ \mathrm{nm}$. Therefore there is only one grid point in the z direction of the magnetic film. For real 3D simulations, we consider a finer meshsize $20\ \mathrm{nm} \times 20\ \mathrm{nm} \times 5\ \mathrm{nm}$, and hence there are 4 grid points in the z direction of the film. In absence of the applied magnetic field, the magnetization in the magnetic film is again relaxed to the stable flower state in Fig. 5(a), with the evolution of the LL energy $\mathcal{F}[\mathbf{M}]$ and the total energy $\mathcal{J}[\mathbf{M}]$ plotted in Fig. 7, and the relaxation dynamics shown in Fig. 5(a). The parameters used in simulations are: the damping constant $\alpha = 0.02$, the characteristic inertial time $\tau = 1.0 \times 10^{-11}$ s, the total simulation time $T = 2$ ns, and the time stepsize $\Delta t = 10$ fs. Due to the simultaneous contributions of the stray field and the inertial term, the performance of the LL energy and the total energy are distinct from that in Fig. 4. Specifically, the LL energy and the total energy generated by the iLLG equation decay over a long period of time, but with oscillations at sub-picosecond timescales.

Remark 4.1. When the stray field is turned on, the homogeneous profile $\mathbf{m}^0 = \mathbf{e}_1$ is no longer an equilibrium state of a ferromagnetic sample. Therefore, the inertial effect is activated at the timescale of sub-picosecond when the system relaxes toward the equilibrium. Furthermore, a nonlinear response to the stray field arises due to highly nonlocal features of both the inertial effect and the stray field. The non-monotonic decrease of both the LL energy and the total energy Fig. 7 results from the nonlinearity. It will be shown later in Fig. 12 that the behaviours of the LL energy are remarkably different when the inertial effect is activated by the applied pulses. In comparison with Fig. 4, these results reveal that the oscillation of the LL energy is mainly determined by the response to the dipolar energy when the inertia is activated.

As demonstrated above, the inertial dynamics governed by the iLLG equation can be activated by a high-frequency magnetic pulse. To establish a quantitative connection between the inertial dynamics and material parameters, only one material parameter

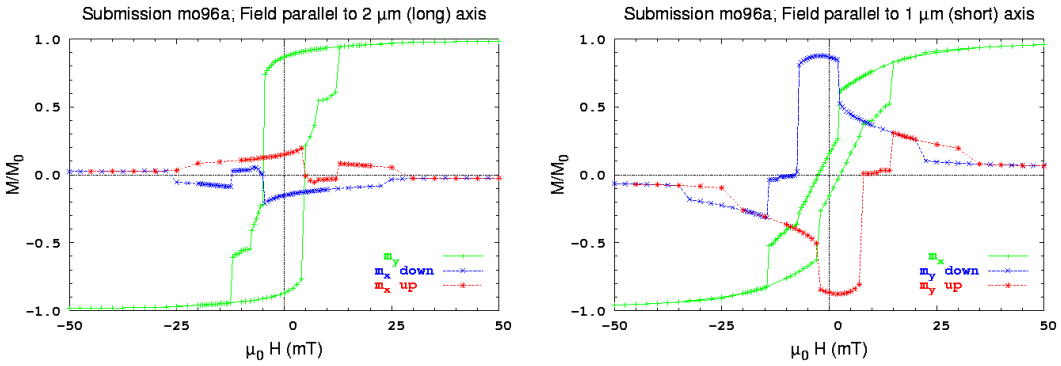

(a) LLG equation: mo96a [19]

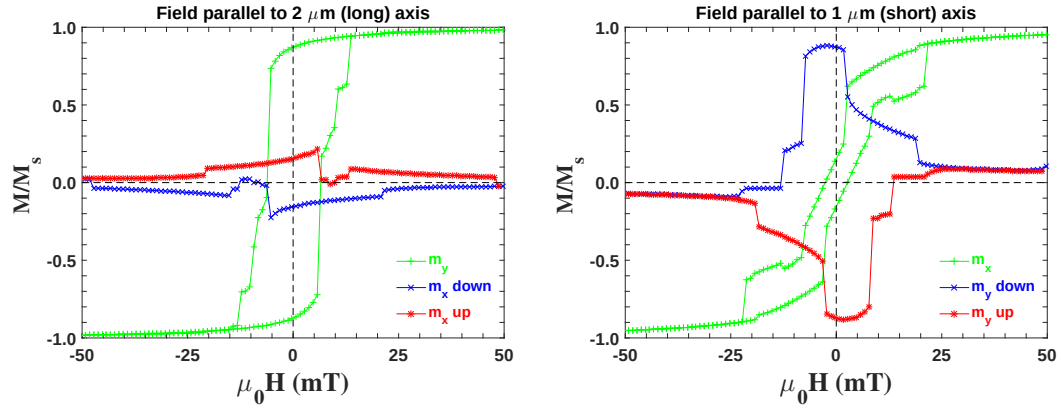

(b) iLLG equation: $\alpha = 0.1$, $\tau = 1.0 \times 10^{-12}$ s, $\Delta t = 1$ ps

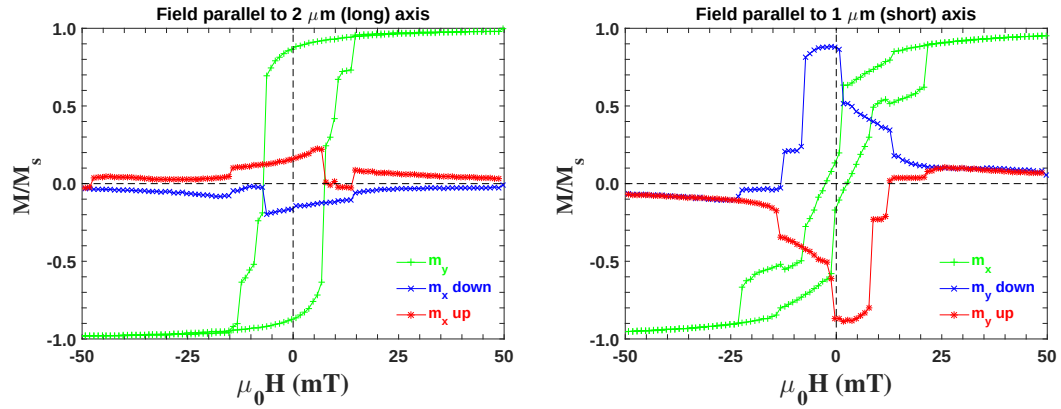

(c) iLLG equation: $\alpha = 0.02$, $\tau = 1.0 \times 10^{-13}$ s, $\Delta t = 0.1$ ps

Figure 6: Hysteresis loops of magnetization simulated by (a) the LLG equation (mo96a) in the standard reference [19], (b) the iLLG equation with the damping parameter $\alpha = 0.1$ and the inertial parameter $\tau = 1.0 \times 10^{-12}$ s, and (c) the iLLG equation with $\alpha = 0.02$ and $\tau = 1.0 \times 10^{-13}$ s. The green/blue/red lines plot the components of magnetization m_y, m_x (down) and m_x (up), respectively. In the left (right) column, an external magnetic field is applied parallel to the 2 μm (1 μm) axis with canting of $+1^\circ$, respectively.

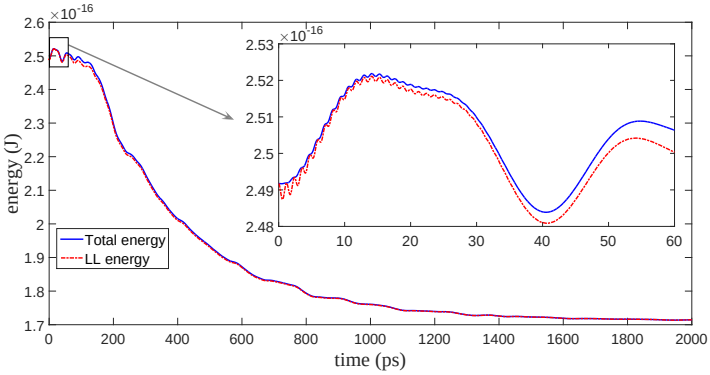

Figure 7: Evolution of the LL energy and the total energy in the relaxation process from a uniform initial state $\mathbf{m}^0 = \mathbf{e}_1$ to the flower state in Fig. 5(a). The ferromagnet of the size $2\ \mu\text{m} \times 1\ \mu\text{m} \times 0.02\ \mu\text{m}$ is discretized to cells with a meshsize $20\ \text{nm} \times 20\ \text{nm} \times 5\ \text{nm}$. The material parameters are: the damping constant $\alpha = 0.02$, the characteristic inertial time $\tau = 1.0 \times 10^{-11}\text{s}$, the total time $T = 2\text{ns}$, and the time stepsize $\Delta t = 10\text{fs}$.

is changed at a time in the simulations, while all other parameters are fixed unless otherwise stated. The magnetic pulses are applied to the material with the initialization of magnetization $\mathbf{m}^0 = \mathbf{e}_1$, so that it relaxes to the equilibrium flower state in Fig. 5(a) under the effects of both the stray field and the inertial term simultaneously.

- The frequency of the magnetic pulse is applied as: $f = 200$ GHz, 500 GHz, and 1000 GHz, respectively. Time evolution of the spatially averaged magnetization and the total energy for the iLLG equation in response to the magnetic pulses are plotted in Fig. 9. We can observe the inertial dynamics of the magnetization and

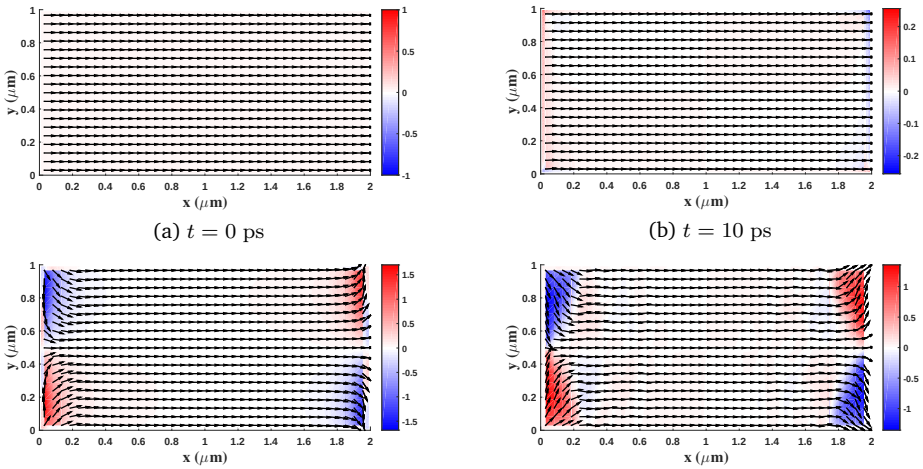

(a) $t = 0$ ps (b) $t = 10$ ps

(c) $t = 0.1$ ns (d) $t = 1$ ns

Figure 8: Evolution of the magnetization profile in the relaxation process from a uniform initial state $\mathbf{m}^0 = \mathbf{e}_1$ to the flower state in Fig. 5(a). The arrow represents the in-plane magnetization and the background color encodes the angle between the in-plane magnetization and the x-axis.

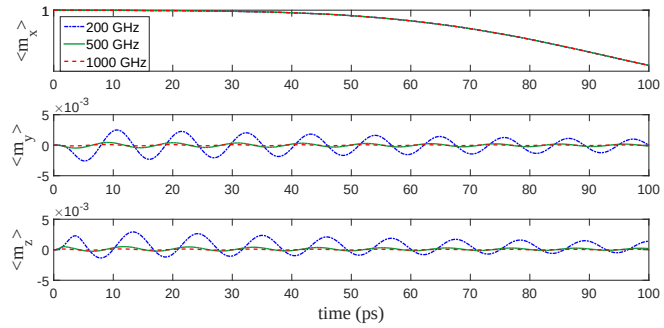

(a) Spatially averaged magnetization

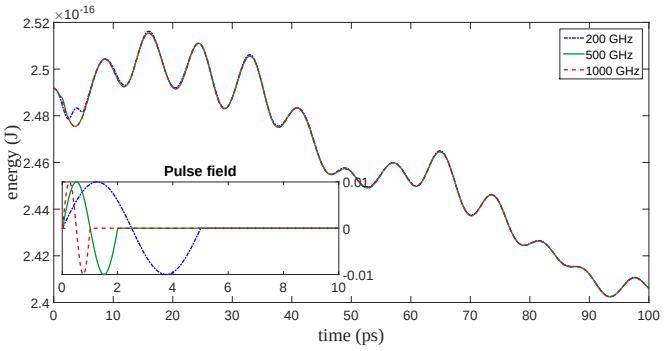

(b) LL energy

Figure 9: Responses of (a) the averaged magnetization (b) LL energy to magnetic field pulses of different frequencies. The dotdashed/solid/dashed lines are for magnetic field pulses with frequencies of 200 GHz, 500 GHz and 1000 GHz, respectively. In the simulation, the damping parameter is $\alpha = 0.02$, and the inertial parameter is $\tau = 1.0 \times 10^{-12}$s.

the oscillation of the LL energy as well. Unlike Figs. 4 and 7, results in Fig. 9 show the existence of the inertial dynamics even in the presence of the stray field. However, as the frequency of the magnetic pulse increases, the inertial dynamics gradually becomes invisible. Meanwhile, it should be mentioned that the LL energy $\mathcal{F}[\mathbf{M}]$ shows small oscillations in an independent frequency with respect to the applied magnetic field pulse.

- The characteristic inertial time τ is fixed to be 1.0×10^{-10} s, and the damping constant varies: $\alpha = 0.005, 0.02, 0.1$. In the presence of a 500 GHz magnetic pulse over $0 \sim 2$ ps, we plot the averaged magnetization as a function of time for the iLLG equation in Fig. 10. As shown in Fig. 10, the smaller the damping parameter is, the more oscillatory the inertial dynamics is.

- The damping parameter α is fixed to be 0.02, and the characteristic inertial time is changed: $\tau = 1.0 \times 10^{-9}$ s, 1.0×10^{-10} s, 1.0×10^{-11} s. In Fig. 11, we plot the averaged magnetization in terms of time for the iLLG equation under a 500 GHz magnetic pulse when $\Delta t = 10$ fs. It is found that more significant oscillation arises for a smaller characteristic inertial time τ.

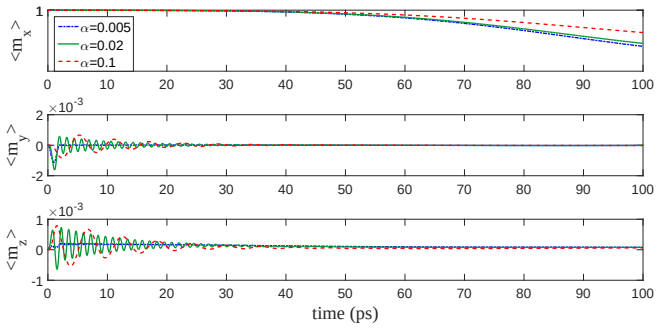

Figure 10: Responses of the averaged magnetization to a 500 GHz magnetic field pulse. The dashed/dotted/solid lines are for damping parameters $\alpha = 0.1$, 0.02 and 0.005, respectively.

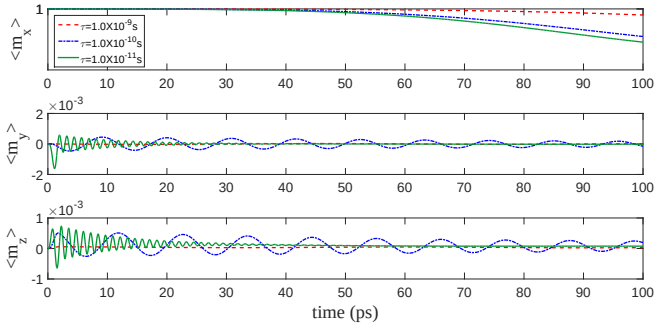

Figure 11: Responses of the averaged magnetization to a 500 GHz magnetic field pulse. The dashed/dotted/solid lines are for characteristic inertial times $\tau = 1.0 \times 10^{-9}$ s, 1.0×10^{-10} s and 1.0×10^{-11} s, respectively.

Remark 4.2. From the mathematical expression of the iLLG equation, it can be inferred that the inertial effect depends on both the damping parameter and the inertial parameter, which have been investigated experimentally in [17, 20]. Meanwhile, the inertial effect can be observed in simulations when τ lies in the range of sub-picosecond and picosecond (10^{-13} s $\sim$ 10^{-10} s), in consistency with physical experiments. Furthermore, it seems that the damping parameter determines the frequency of the oscillation in magnetization at sub-picosecond timescales.

Finally, we consider an initial magnetic profile where the stray field is fully relaxed. Such an equilibrium state is obtained from the homogeneous state $\mathbf{m}^0 = \mathbf{e}_1$ for a relaxation time of $T = 2$ ns with following parameters: the damping constant $\alpha = 0.1$, the characteristic inertial time $\tau = 1.0 \times 10^{-12}$ s, and the time stepsize $\Delta t = 1$ ps. Based on this fully relaxed magnetic profile, a magnetic field pulse of 500 GHz is then applied with modified parameters: $\alpha = 0.005$, $\tau = 5.0 \times 10^{-11}$ s, and $\Delta t = 0.1$ ps. In Fig. 12, the oscillating magnetization with a frequency around 620 GHz is clearly observable, which lasts until 250 ps.

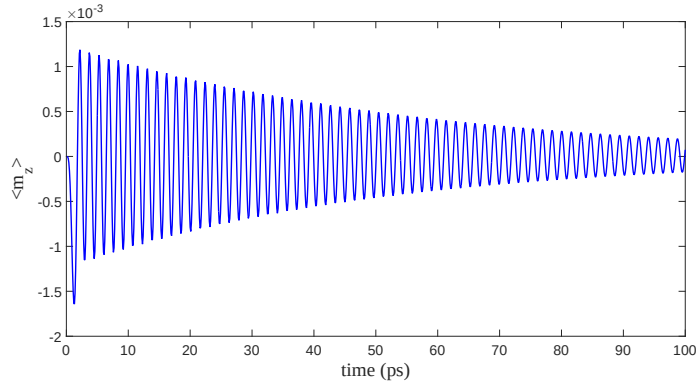

(a) Spatially averaged magnetization

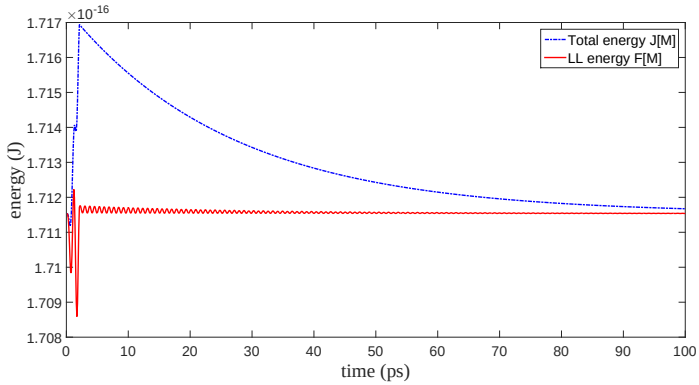

(b) Total energy and LL energy

Figure 12: Responses of (a) the spatially averaged magnetization and (b) LL energy to a 500 GHz magnetic pulse field. The initial state of the simulation is the stable flower state in Fig. 5(a), prepared by relaxing the uniform magnetization state $\mathbf{m}^0 = \mathbf{e}_1$.

5. Conclusion

In this work, we propose a second-order semi-implicit scheme for the inertial Landau-Lifshitz-Gilbert equation, to study the ultrafast inertial dynamics of ferromagnetic materials at sub-picosecond timescales. The unique solvability of the proposed method is theoretically proved, and the dependence of the number of iterations in GMRES for solving the unsymmetric linear system of equations on the damping/inertial parameters is explored and further verified by numerical tests. Micromagnetics simulations show that the inertial Landau-Lifshitz-Gilbert equation hosts inertial effects at sub-picosecond timescales, but gives rises to basically the same magnetic dynamics as the Landau-Lifshitz-Gilbert equation for larger timescales. Moreover, the dependence of the inertial dynamics on the frequency of the applied field, the damping parameter, and the inertial parameter are systematically investigated. These studies shall be helpful in designing magnetic devices with ultrafast magnetization dynamics of non-negligible inertial behavior.

Acknowledgments

P. Li is grateful to Kelong Zheng for helpful discussions, and is also grateful for the discussions with Changjian Xie and Yifei Sun on coding.

P. Li is supported by the Postgraduate Research & Practice Innovation Program of Jiangsu Province (Grant No. KYCX20_2711). L. Yang is supported by the Science and Technology Development Fund, Macau SAR (Grant No. 0070/2019/A2) and the National Natural Science Foundation of China (NSFC) (Grant No. 11701598). J. Lan is supported by NSFC (Grant No. 11904260) and the Natural Science Foundation of Tianjin (Grant No. 20JCQNJC02020). R. Du was supported by NSFC (Grant No. 11501399). J. Chen is supported by NSFC (Grant No. 11971021).

References

[1] S. Bartels and A. Prohl, *Convergence of an implicit finite element method for the Landau-Lifshitz-Gilbert equation*, SIAM J. Numer. Anal. 44 (2006), 1405–1419.

[2] E. Beaurepaire, J.-C. Merle, A. Daunois, and J.-Y. Bigot, *Ultrafast spin dynamics in ferromagnetic nickel*, Phys. Rev. Lett. 76 (1996), 4250–4253.

[3] S. Bhattacharjee, L. Nordström, and J. Fransson, *Atomistic spin dynamic method with both damping and moment of inertia effects included from first principles*, Phys. Rev. Lett. 108 (2012), 057204.

[4] A. Brataas, A. D. Kent, and H. Ohno, *Current-induced torques in magnetic materials*, Nat. Mater. 11 (2012), 372–381.

[5] Center for applied scientific computing, Lawrence livermore national laboratory, *Hypre: scalable linear solvers and multigrid methods*, 1952.

[6] J. Chen, C. Wang, and C. Xie, *Convergence analysis of a second-order semi-implicit projection method for Landau-Lifshitz equation*, Appl. Numer. Math. 168 (2021), 55–74.

[7] I. Cimrák, *Error estimates for a semi-implicit numerical scheme solving the Landau-Lifshitz equation with an exchange field*, IMA J. Numer. Anal. 25 (2005), 611–634.

[8] I. Cimrák, *A survey on the numerics and computations for the Landau-Lifshitz equation of micromagnetism*, Arch. Comput. Methods Eng. 15 (2008), 277–309.

[9] M.-C. Ciornei, J. M. Rubí, and J.-E. Wegrowe, *Magnetization dynamics in the inertial regime: Nutation predicted at short time scales*, Phys. Rev. B 83 (2011), 020410.

[10] T. Gilbert, *A Lagrangian formulation of gyromagnetic equation of the magnetization field*, Phys. Rev. 100 (1955), 1243–1255.

[11] M. Kammerer, M. Weigand, M. Curcic, M. Noske, M. Sproll, A. Vansteenkiste, B. V. Waeyenberge, H. Stoll, G. Woltersdorf, C. H. Back, and G. Schuetz, *Magnetic vortex core reversal by excitation of spin waves*, Nat. Commun. 2 (2011), 1–6.

[12] S. K. Kim, K. Nakata, D. Loss, and Y. Tserkovnyak, *Tunable magnonic thermal hall effect in skyrmion crystal phases of ferrimagnets*, Phys. Rev. Lett. 122 (2019), 057204.

[13] M. Kruzík and A. Prohl, *Recent developments in the modeling, analysis, and numerics of ferromagnetism*, SIAM Rev. 48 (2006), 439–483.

[14] J. Lan, W. Yu, and J. Xiao, *Geometric magnonics with chiral magnetic domain walls*, Phys. Rev. B 103 (2021), 214407.

[15] L. Landau and E. Lifshitz, *On the theory of the dispersion of magetic permeability in ferromagnetic bodies*, Phys. Z. Sowjetunion 8 (1935), 153–169.

[16] P. LI, C. XIE, R. DU, J. CHEN, AND X.-P. WANG, *Two improved Gauss-Seidel projection methods for Landau-Lifshitz-Gilbert equation*, J. Comput. Phys. 401 (2020), 109046.
[17] Y. LI, A.-L. BARRA, S. AUFFRET, U. EBELS, AND W. E. BAILEY, *Inertial terms to magnetization dynamics in ferromagnetic thin films*, Phys. Rev. B 92 (2015), 140413.
[18] F. MANFRED, S. DANIEL, AND I. CHRISTIAN, *Generalized Gilbert equation including inertial damping: Derivation from an extended breathing Fermi surface model*, Phys. Rev. B 84 (2011), 172403.
[19] MICROMAGNETIC MODELING ACTIVITY GROUP, *National institute of standards and technology*, `https://www.ctcms.nist.gov/rdm/mumag.org.html`, 2000.
[20] K. NEERAJ ET AL., *Inertial spin dynamics in ferromagnets*, Nat. Phys. 17 (2021), 245–250.
[21] M. RUGGERI, *Numerical analysis of the Landau-Lifshitz-Gilbert equation with inertial effects*, ESAIM: Math. Model. Numer. 56 (2022), 1199–1222.
[22] Y. SAAD AND H. S. MARTIN, *GMRES: A generalized minimal residual algorithm for solving nonsymmetric linear systems*, SIAM J. Sci. Comput. 7 (1986), 856–869.
[23] Y. SUN, J. CHEN, R. DU, AND C. WANG, *Advantages of a semi-implicit scheme over a fully implicit scheme for Landau-Lifshitz-Gilbert equation*, arXiv:2106.06936, (2021).
[24] X.-P. WANG, C. J. GARCÍA-CERVERA, AND W. E, *A Gauss-Seidel projection method for micromagnetics simulations*, J. Comput. Phys. 171 (2001), 357–372.
[25] C. XIE, C. J. GARCÍA-CERVERA, C. WANG, Z. ZHOU, AND J. CHEN, *Second-order semi-implicit projection methods for micromagnetics simulations*, J. Comput. Phys. 404 (2020), 109104.
[26] I. ŽUTIĆ, J. FABIAN, AND S. DAS SARMA, *Spintronics: Fundamentals and applications*, Rev. Mod. Phys. 76 (2004), 323–410.